Electronic Supplementary Material (ESI) for Sustainable Energy & Fuels.

Supplementary Information for

Oxygen Vacancies Coupled with Surface Silicide Facilitate the CO_2 Activation at Near-Room Temperature for Efficient Methane Productivity on Ni-Oxide Supported Pd Nanoparticles

Thomas Yang,[1‡] Amisha Beniwal,[1‡] Dinesh Bhalothia,[1*] Che Yan,[1] Chia-Hsin Wang,[2] and Tsan-Yao Chen, 1[*]

Affiliations:

[1] Department of Engineering and System Science, National Tsing Hua University, Hsinchu 30013, Taiwan

[2] National Synchrotron Radiation Research Center, Hsinchu 30076, Taiwan

‡ denotes the equal contribution of authors.

Corresponding Author(s):

Tsan-Yao Chen
Email: chencaeser@gmail.com
Tel: +886-3-5715131 # 34271
FAX: +885-3-5720724

Dinesh Bhalothia
Email: fortuner2014@gmail.com

1. Transmission electron microscopy inspection of control samples.

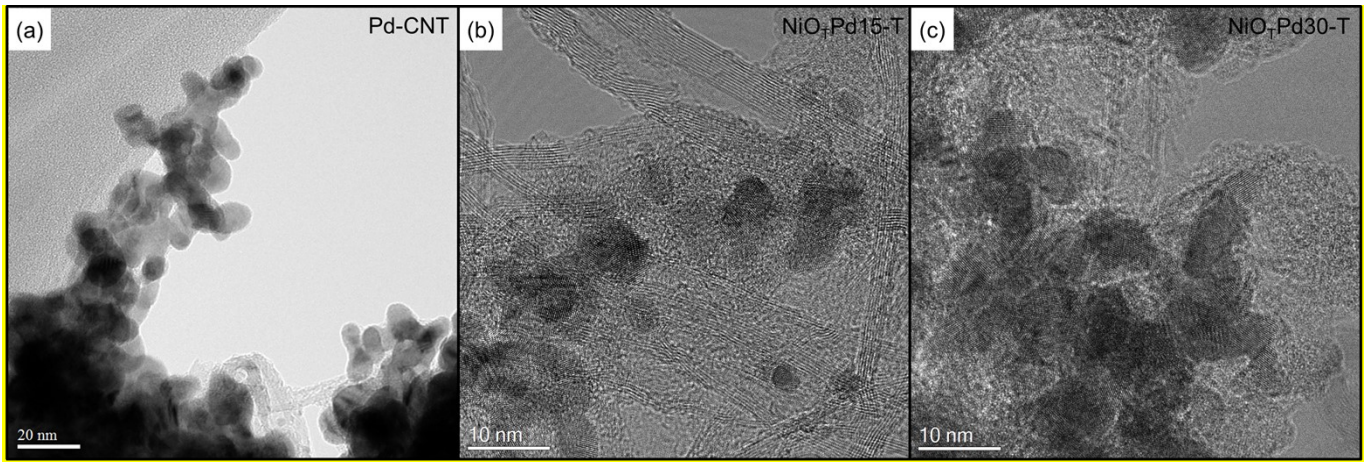

Figure S1. Low-resolution HRTEM images of (a) as-prepared Pd-CNT, (b) NiO$_T$Pd15-T and (c) NiO$_T$Pd30-T NCs.

2. X-ray diffraction analysis on the experimental samples

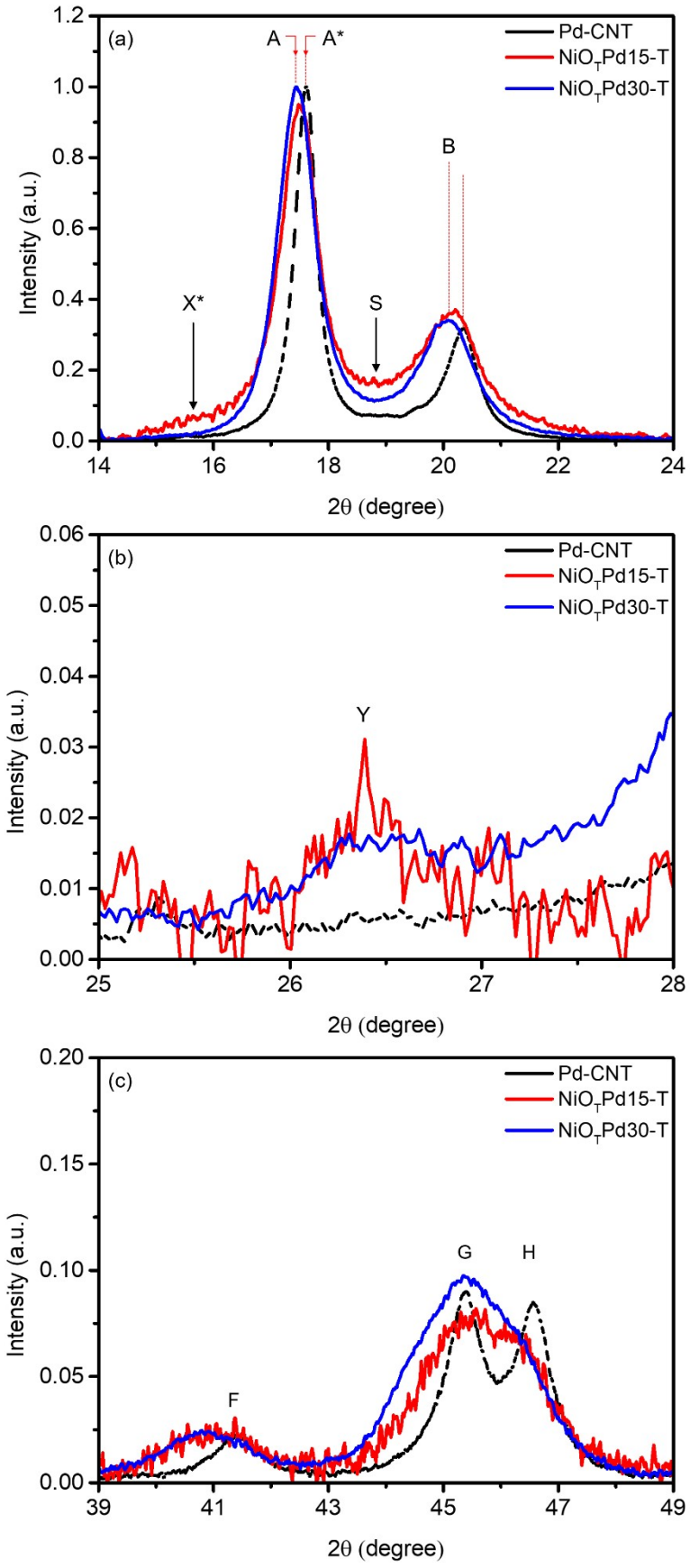

Figure S2. The zoom in regions of (i), (ii) and 39^o – 49^o for the diffraction patterns in Figure 2.

Table S1. The d-spacing and intensity ratio of the diffraction peak from (111) to (hkl) facets for the experimental samples (NiO_TPd15-T and NiO_TPd30-T) and reference sample (Pd-T).

Facets	Lattice space (Å)			H(111)/H(hkl)			Delta d vs. Pd-CNT (%)	
	Pd-CNT	NiO_TPd15-T	NiO_TPd30-T	Pd-CNT	NiO_TPd15-T	NiO_TPd30-T	Δd - 15T	Δd - 30T
(111)	2.25	2.265	2.27	1	1	1	0.64	0.87
(200)	1.951	1.969	1.977	3.35	2.77	3.04	0.9	1.33
(220)	1.377	1.385	1.39	4.37	5.16	4.69	0.58	0.95
(311)	1.175	1.183	1.187	3.98	4.42	4.31	0.68	1.06
(222)	1.125	1.13	1.136	11.90	14.97	15.70	0.5	0.97

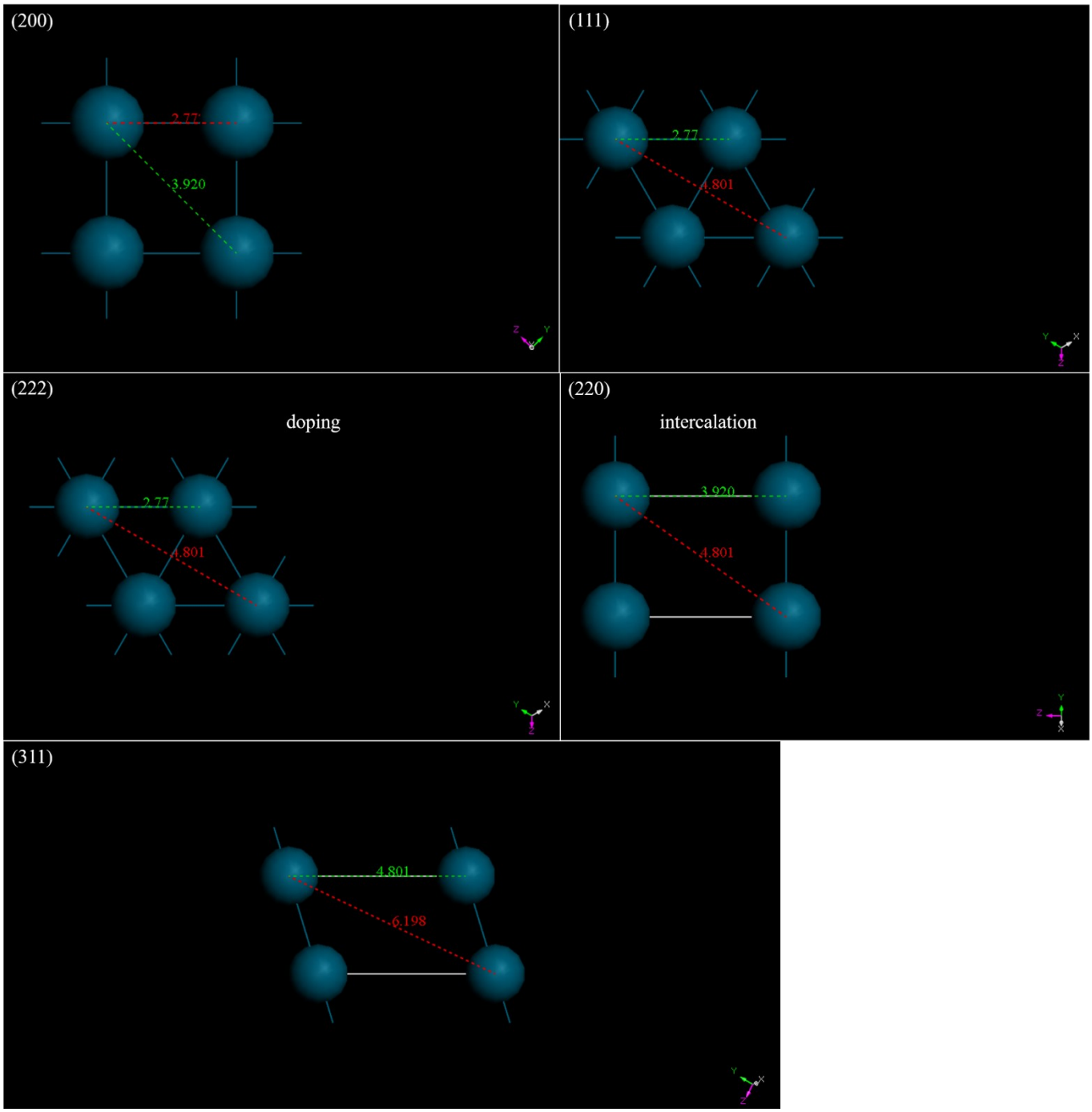

Figure S3. The surface atomic arrangement of (111), (200), (220), (311) and (222) facets of fcc phase Pd crystal.

3. X-ray absorption analysis of the Atomic structure of control samples

X-ray absorption spectroscopic analysis is employed to elucidate the local atomic structure around Pd atoms of the experimental samples. For clarifying the effects of Pd-Ni hybridization and the TMOS in Ni oxide supported Pd NCs, results of the monometallic Pd and Ni NCs with the same surface modification as that of experimental samples are compared in Figure S4. The corresponding results resemble that the local atomic structure of Pd NC is disordered by the formation of a thin Pd oxide layer in the presence of TMOS on its surface. On the other hand, the local structure symmetry around Ni atoms is improved by the same treatment on NiO_T-T. These characteristics reveal the selectivity of metallic Pd atom is higher than that of Ni to the TMOS molecule.

In **Figure S4a**, with the same position of inflection point (X) as that of Pd powder (**Figure S4a**, inset), the Pd atoms in Pd-CNT and Pd-T preserve a metallic state. Consequently, compared with that of Pd powder, the lifting of valley V with the suppression of absorption peak height (H_N) and the narrowing of the width between the two-absorption peaks (W_{MN}) can be attributed to the oxygen adsorption on the surface atoms of the Pd-CNT. In terms of Pd-T, compared to that of Pd-CNT, the further suppression of H_N with narrowing of W_{MN} is due to the formation of a thin Pd oxide layer on the NC surface and is consistently revealed by the substantially suppressed radial peak B (ΔH_B) in **Figure S4b** corresponding to a decrement of coordination number for Pd-Pd bond pairs ($CN_{Pd\text{-}Pd}$) by 1.53 (i.e, 20.5%).

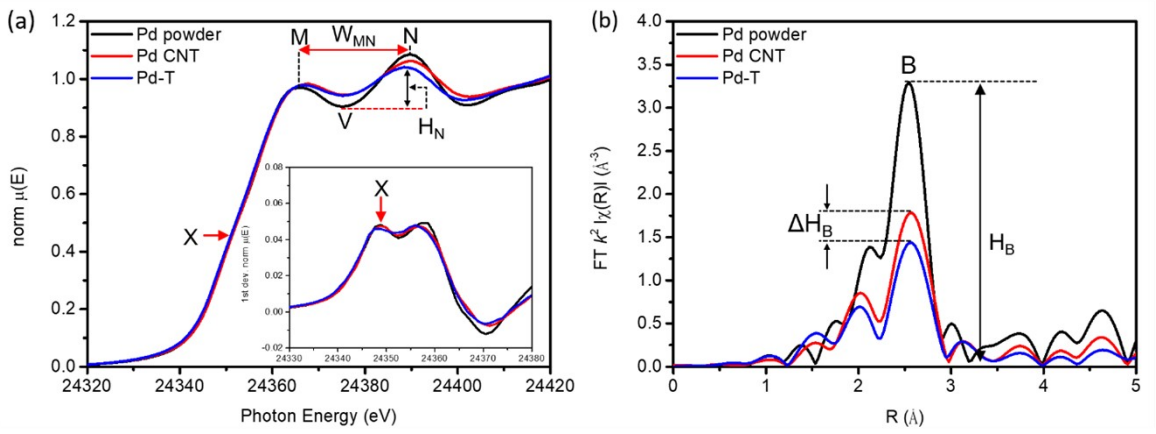

Figure S4. (a) The X-ray absorption near edge structure (XANES) spectra and (b) the corresponding Fourier transformed extended X-ray absorption fine structure (EXAFS) spectra of standard Pd powder, Pd-CNT and Pd-T NCs at Pd K-edge.

The XANES spectra of monometallic Ni oxides (i.e., NiO_T and NiO_T-T) and Ni foil are demonstrated in **Figure S5a**. As shown, with the same inflection point (X) to that of NiO_T, the same profile in both near-edge peak (C) and deviation curve (inset) suggest that the chemical state of Ni atoms remains unchanged by interacting with TMOS in NiO_T-T. Meanwhile, as compared to that of NiO_T, the suppression of background intensity with an increased height (H_X) to width (W_X) ratio of the pre-edge peak (**Figure S5b**) suggests the improvement of local symmetry around Ni atoms in NiO_T-T. **Figure S5c** demonstrates the corresponding EXAFS spectra and the quantitative atomic structure parameters from the model analysis are summarized in **Table S3**. Accordingly, compared to that of NiO_T, the coordination number for the oxygen atom in the 1st atomic shell of Ni atom (CN_{Ni-O1}) is increased by 0.5 while that of Ni and O atoms is changed respectively by 0.14 and -1.07 in the 2nd atomic shell of NiO_T-T. In the absence of direct bonding to the Si atom in the first coordination shell (CN_{Ni-Si}), the decoration is formed by the adsorption followed by hydration of TMOS into silicate on the NiO_T-T surface. Such a scenario results in the Si-O-Ni bonding between silicate, therefore, suppressing the CN_{Ni-O2} as well as the long-range ordering around Ni atoms.

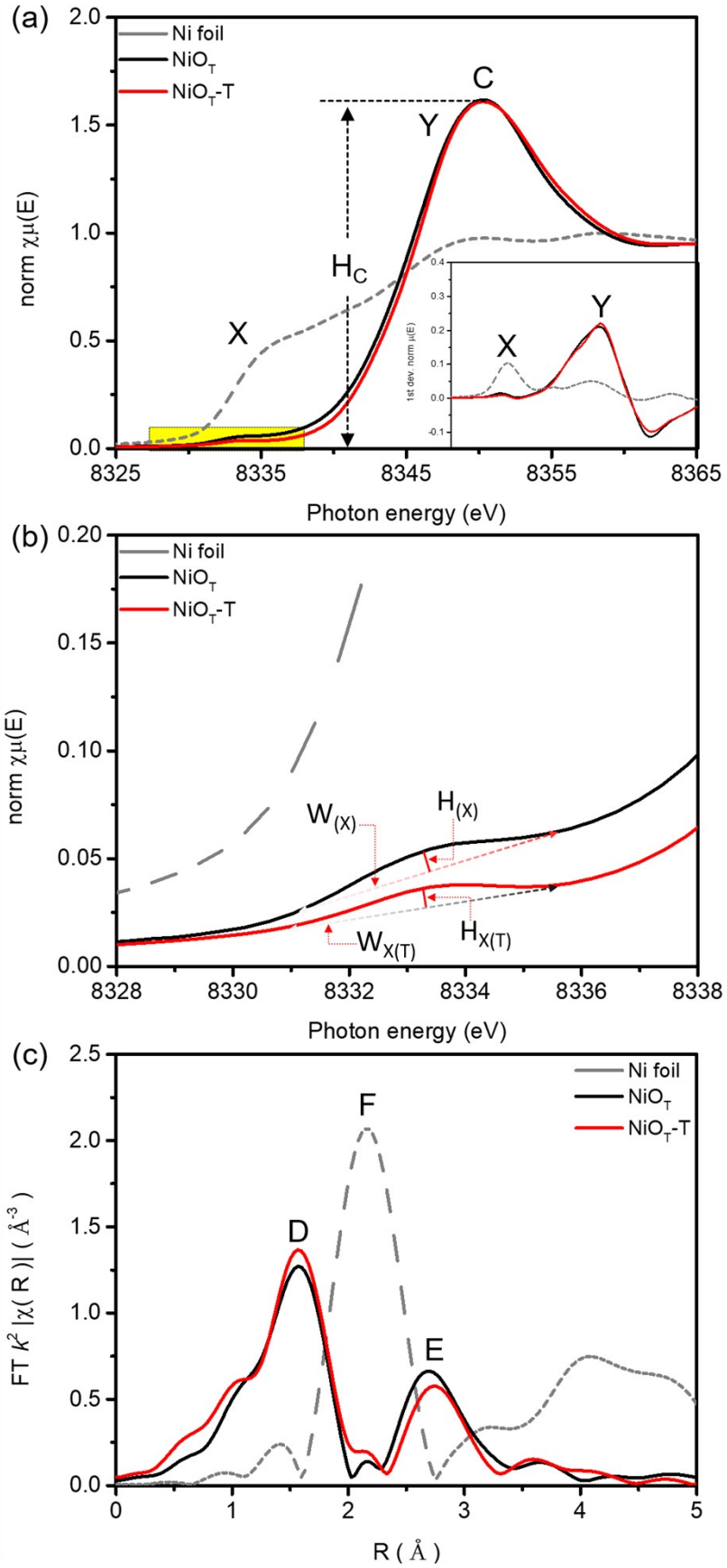

Figure S5. (a) The X-ray absorption near edge structure (XANES) spectra (b) the room-in of region X and (c) the corresponding Fourier transformed extended X-ray absorption fine structure (EXAFS) spectra of standard Ni foil, NiO_T and NiO_T-T NCs at Ni K-edge.

Figure S6a and **inset** respectively compare the Ni K-edge XANES spectra and corresponding 1st deviation curves of the NiO_TPd15-T with that of the Ni foil, NiO_T and the NiO_TPd15. In a XANES spectrum, the position of the inflection point X (Y) resembles the threshold energy for the electron transition from 1s to 3d (4s/4p) orbitals and the intensity of the near-edge (H_C) peak refers to the extent of 4s/4p empty state of Ni atoms. The former is proportional to the extent of the oxidation state and the latter is the index for the extent of electron transition from Ni to the neighboring atoms. For further clarification, the zoom-in of the pre-edge region is demonstrated in **Figure S7a** and corresponding parameters are summarized in **Table S2,** where the intensity to width ratio in the pre-edge region (H_X/W_X) is the index for the extent of orbital distortion (i.e., local atomic structure symmetry). As depicted in **Figure S6a**, compared to that of NiO_T, a suppression of H_C by 19.2% (from 1.61 to 1.30) with an enhancement of H_X/W_X by 0.05 (**Figure S7a** and **Table S2**) respectively suggest the increased electron density in the 4s/4p orbitals and the improved local atomic symmetry around the Ni atoms in NiO_TPd15. These scenarios could be rationalized by the preservation of certain metallic Ni atoms in the interface between the Pd nano-islands and the Ni oxide. Compared to the near-edge features of the NiO_TPd15, by decorating with TMOS molecule followed by the hydration reaction, a substantially enhanced H_C by 26.9% (from 1.30 to 1.65), the broadening of peak C with a slight shift to high energy and the suppression of H_X/W_X ratio by 0.05 respectively refer to the electron relocation to the neighboring atoms, the expansion and chemical shift of 4s/4p band to high energy and the disordering of local symmetry around the Ni atoms in the NiO_TPd15-T. In addition, the presence of a shoulder in the low energy side of peak Y in the inflection curve indicates the splitting of 4s/4p orbitals and can be attributed to the formation of a strong chemical bond with Si atoms in the Pd silicide. Results of NCs with a Pd/Ni ratio of 3.0 are compared in **Figure S6b** and **Table S2**. Compared to that of NiO_TPd15, with the same position of X, a substantially increased H_C by 0.22 (16.7%) and lower H_X/W_X ratio indicate a higher extent of electron relocation and lower extent of local atomic structure symmetry from Ni to the neighboring atoms in the NiO_TPd30 (**Figure S7b**). Such a scenario seemly controversial to higher coverage of Pd nano-island on the Ni oxide (**Figure S1**), however, consistently rationalizes the results of XRD analysis in which a high content of galvanic replacement between Pd^{2+} ions

and Ni atoms followed by the co-precipitation of Ni and Pd atoms into Pd-riched crystal and the subsequent oxidation of Ni atoms in its surface. Consequently, with a higher surface exposure of Ni atoms to that of NiO_TPd15, a higher extent of Ni oxidation with a lower local atomic symmetry to oxygen atoms (shown by the suppressed H_X/W_X). For NiO_TPd30-T, compared to the spectroscopic feature of NiO_TPd30, a higher H_C and splitting of deviation peak (depicted by a weak shoulder on the low energy side of peak Y) with a pronounced intensity respectively denote the further oxidation of Ni atoms and formation of Pd silicide.

For a detailed inspection of the atomic structure and local symmetry, the FT-EXAFS curves for NCs with Pd/Ni ratios of 1.5 and 3.0 are, respectively, demonstrated in **Figure S6c** and **Figure S6d**; where the radial peaks D and E are contributions of the X-ray interferences respectively to the atomic bond pairs to O atom in the 1st coordination shell (Ni-O1) as well as the Ni and O atoms in the 2nd coordination shell (Ni-Ni2 and Ni-O2). Meanwhile, the atomic structure parameters of all samples from the model analysis are compared in **Table S3**. As depicted in **Figure S6c**, compared to that of NiO_T, the upshift of peak D to D* indicates the elongation of Ni-O1 distance by 0.09 Å, therefore, increasing the local space for the relaxation of neighboring atoms (oxygen and Ni) around the Ni atoms in NiO_TPd15. Such a scenario is attributed to the intercalation of Pd atoms which induces a certain extent of oxygen defects and is elucidated by suppression of $CN_{Ni\text{-}O1}$ by 1.34 to 3.44 (**Table S3**) in the first coordination shell around the Ni atoms in the Ni oxide. Competition of reaction kinetics for the galvanic replacement to that of the heterogeneous nucleation and crystal growth of Pd nano-island could be a potential rationale. With a low content of Pd^{2+} ions, the reaction kinetics of galvanic replacement to Ni atoms in the Ni oxide is suppressed and thus results in a limited amount of residual Ni^{2+} ions (Ni^{2+R}) in the reaction system. Consequently, the steric configuration and composition of the Pd nano-island is dominated by the crystal growth pathway in which a low content of Ni atoms (by interacting Ni^{2+R} with the reduction agent) is intercalated in its surface upon the coprecipitation with the Pd atoms. These hypotheses are further rationalized by the formation of short-range ordered (long-range disordered) Ni oxide illustrated by the substantial suppression on the peak E and the presence of shoulder F* in the FT-EXAFS curve. The former corresponds to the absence of $CN_{Ni\text{-}O2}$ in the 2nd atomic shell. The latter is the contribution of Ni-O and metallic Ni-Ni bond pairs respectively with

a CN of 1.40 and 0.78 at 2.435 and 2.522 Å in the 1st coordination shell of the Ni atoms. Hereby, a slight Ni intermix of 6.5% around Pd atoms with the absence of Pd around Ni atoms (**Table S3**) and the retention of metallic Ni atom rationalize that the NiO_TPd15 NC is composed of sub-nanometer metallic Ni clusters in the interface between the Pd nano-islands and long-range disordered Ni oxide. In which, the Ni atoms are coordinated to oxygen atoms in the tetrahedral symmetry sites with certain extent of oxygen defects. Adsorption of TMOS followed by its hydration reaction with water molecules restructures the atomic arrangement in the NiO_TPd15-T surface. As shown in **Figure S6c**, compared to that of NiO_TPd15, the offset of peak D* to a lower radial position with an enhanced intensity respectively indicate the compression of bond length by 0.099 Å and with the increment of CN_{Ni-O1} by 2.08. Meanwhile, compared to that of NiO_T, a slightly enhanced radial peak * is the contribution of Ni-Si bond pair with a CN_{Ni-Si} of 0.69 at 2.465 Å and is complimentary evidence with the splitting of 1st deviation curve in **Figure S6a** inset for the formation of $NiPd_3$ alloy in the NiO_TPd15-T. In this event, compared to that of NiO_TPd15, the pronounced radial peak E is the contribution of the Ni-O and Ni-Ni bond pairs with the coordination numbers of 2.14 and 2.97, respectively. Since the number of oxygen atoms (CN_{Ni-O2}) is higher than that of the Ni atoms in the 2nd coordination shell (CN_{Ni-Ni2}) in a Ni oxide, such a result is controversial however can be rationalized by the formation of NiPd oxide by the adsorption of TMOS molecules accompanied with the hydration reaction in the metallic Ni atoms. Therefore, compared with that of NC without TMOS decoration (i.e., NiO_TPd15), a reduced CN_{Ni-O2} by 0.83 could be rationalized by co-sharing of oxygen between the Si and Ni atoms (i.e., Si-O-Ni bond) alloying with metallic Ni atoms in the NiO_TPd15-T. The same pathways hold in all samples with the TMOS decoration. Meanwhile, compared to that of Pd atoms, a substantially reduced heteroatomic intermix of Si to Ni atoms suggests the truth for the retention of low contents of metallic Ni atoms in the NiO_TPd15. For the case of NiO_TPd30, compared to that of NiO_T, the suppressed CN in all coordination shells suggest the formation of oxygen defects around Ni atoms by the intercalation of Pd atoms and the growth of Pd riched NiPd nano-island in the Ni oxide surface. Meanwhile, as illustrated by the CN_{Ni-Ni1}, the metallic Ni atoms in the Pd to Ni oxide interface are absent. Consequently, in the NiO_TPd30-T, the $NiPdO_3$ is formed by the interaction of TMOS molecules with the retained Ni atoms in the Pd nano-island

and the oxygen defects in the Ni oxide of the NiO_TPd30. Since the content of metallic Ni atoms in Pd nano-island and the oxygen defect in Ni oxide is low as compared to that of NiO_T15Pd-T, the suppression of $NiPdO_3$ is expectable. For clarification in detail, corresponding model analysis fitting curves of the above NCs are compared with their experimental spectra at Ni and Pd K-edges in **Figure S8**.

The Wavelet transformed EXAFS (WT-EXAFS) pattern of NiO_T, NiO_TPd15, NiO_TPd15-T, NiO_T-T, NiO_TPd30 and NiO_TPd30-T are demonstrated in **Figures S6e to S6j**. The distribution of WT EXAFS pattern in radial and the wavenumber axes correspond respectively to the dispersion of the interatomic distance and the extent of electronic interaction from Ni to the neighboring atoms; where the profiles of the histogram in regions A and B are X-ray interferences between center and the atoms 1^{st} and 2^{nd} nearest coordination shell. As indicated in **Figure S6e**, the extension of the histogram ranging from 1.5 to 2.5 Å consistently reveals the coexistence of the metallic Ni (Ni-Ni) and Ni oxides (Ni-O) bond pairs. Meanwhile, the considerable extent of backscattering intensity with the splitting of pattern in three lines till 5 Å resembles the presence of long-range ordered atomic structure in NiO_T. For NiO_TPd15 (**Figure S6f**), compared to that of NiO_T, the changes of WT pattern in spherical symmetry (denoted by the black arrow) at 1.9 to 2.0 Å and the suppression of the backscattering intensity with narrowing W_X and merging of pattern in region B reveals the formation of short-range ordered local around Ni atoms. By capping silicide on NiO_TPd15-T surface, the extension and enhancement of the WT pattern elucidate the improvement of local structure ordering around N atoms in Ni oxide (**Figure S6g**). The hybridization between Si and Ni atoms is confirmed by the changes of WT pattern symmetry from line dispersion in NiO_T to the droplet like dispersion in NiO_T-T (**Figure S6h**). Such an evolution reveals the difference of the electron relocation manners between the Ni-Si and Ni-O bond pairs due to the electronegativity and electronic configuration of Si and O atoms. Compared with that of NiO_TPd15 and NiO_TPd15-T, the substantially enhanced intensity and expanded W_X are found both in the NiO_TPd30 (**Figure S6i**) and NiO_TPd30-T (**Figure S6j**). Such a scenario indicates the stronger electron localization around Ni atoms (i.e., the lower extent of heteroatomic hybridization to the neighboring Si and O atoms) due to the higher extent of steric protection with thicker Pd nano-islands in the Ni oxide surface.

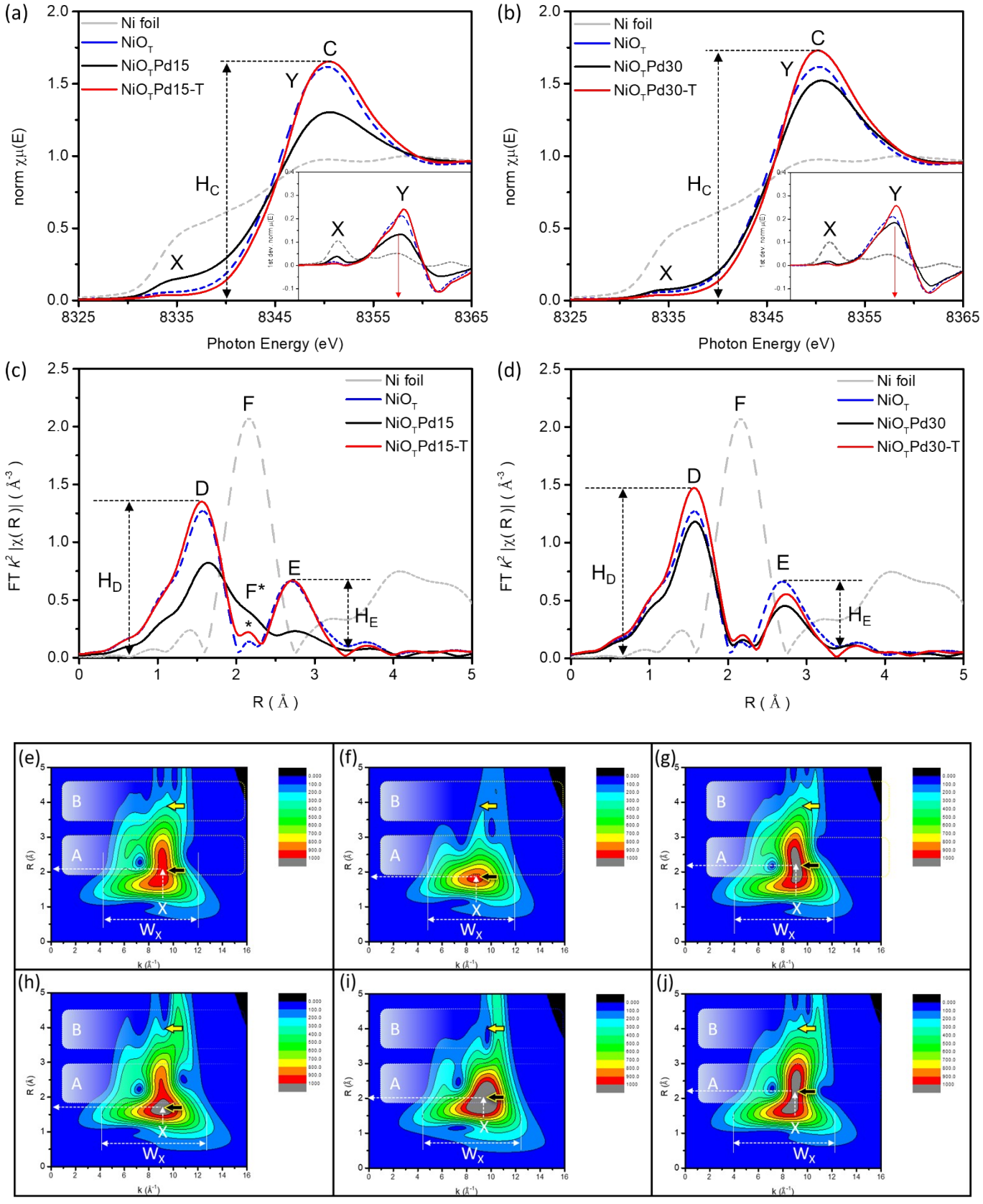

Figure S6. X-ray absorption near-edge structure (XANES) spectra of NiO$_T$-T compared with (a) NiO$_T$Pd15 (without TMOS capping) and NiO$_T$Pd15-T and (b) NiO$_T$Pd30 (without TMOS capping) and NiO$_T$Pd30-T NCs at Ni K-edge. The corresponding Fourier transformed EXAFS spectra are demonstrated in (c) and (d) and the Wavelet transformed (WT) EXAFS patterns are shown in (e) for NiO$_T$, (f) for NiO$_T$Pd15, (g) for NiO$_T$Pd15-T, (h) for NiO$_T$-T, (i) for NiO$_T$Pd30 and (j) for NiO$_T$Pd30-T.

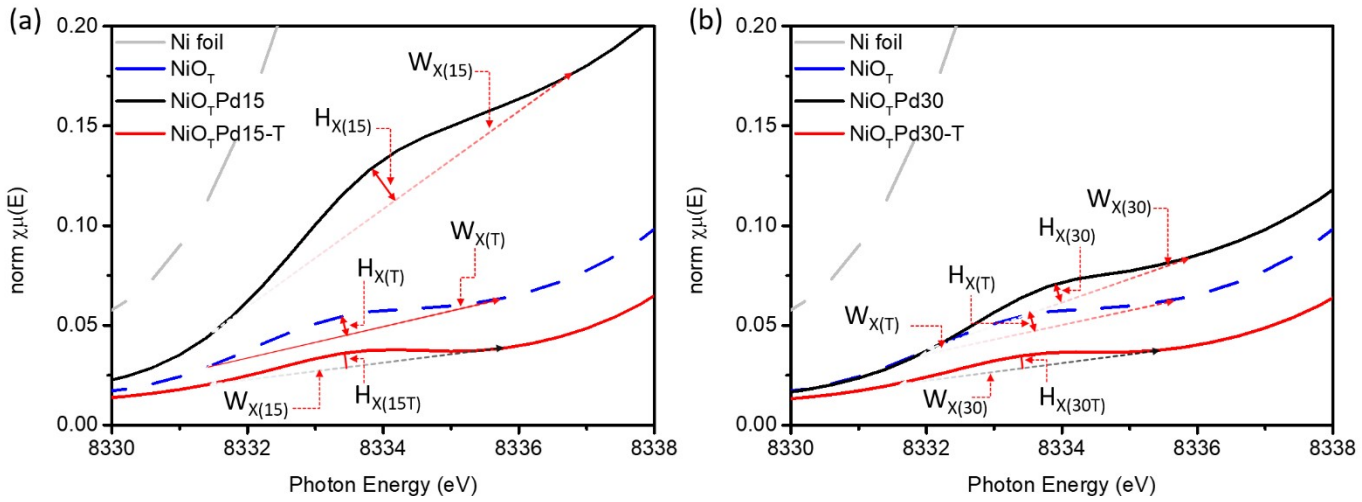

Figure S7. Zoom-in of pre-edge region of Ni K-edge XANES spectra for (a) NiO$_T$Pd15-T and (b) NiOTPd30-T with the control samples without TMOS and reference sample of NiO$_T$.

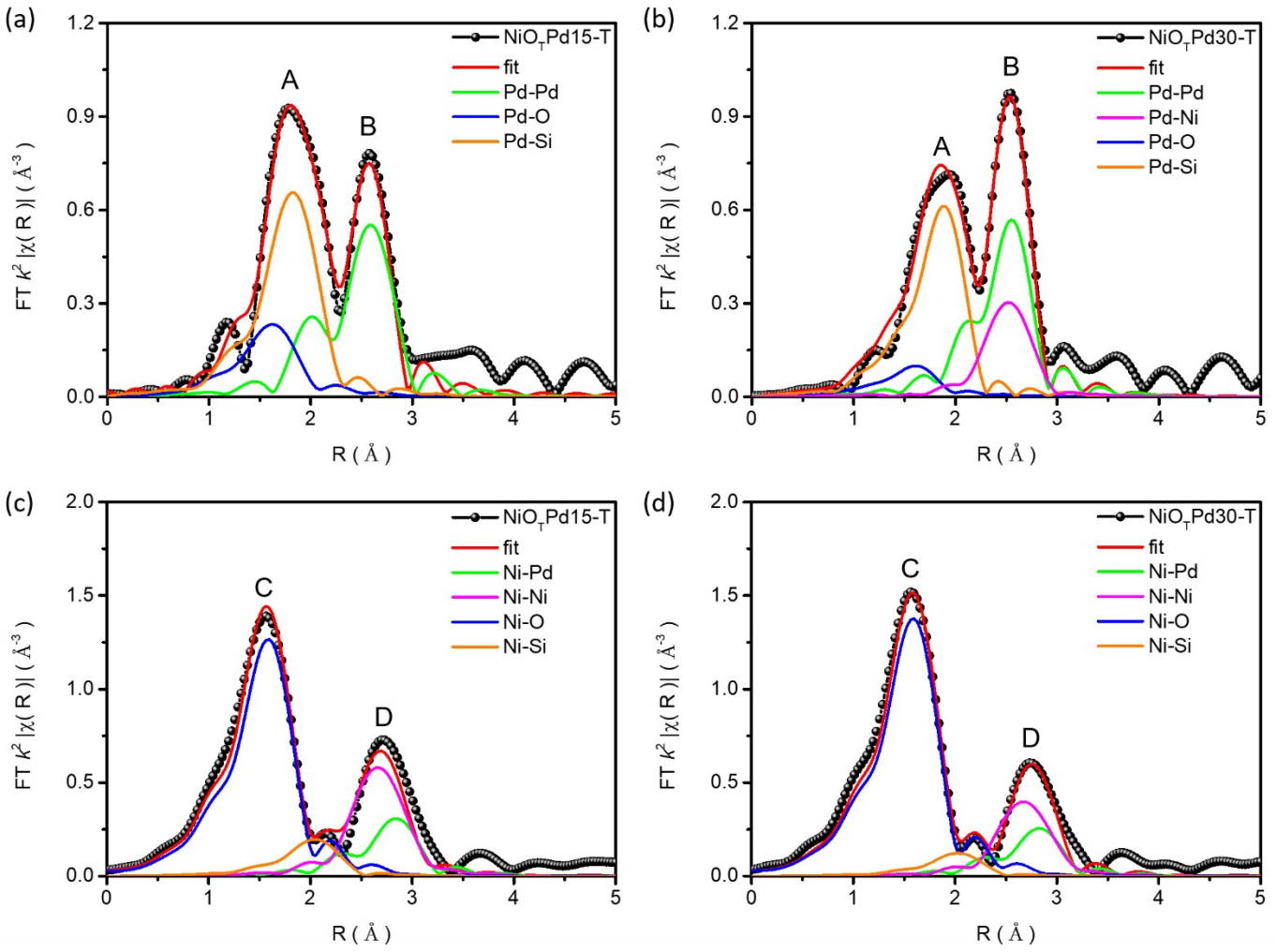

Figure S8. The Fourier transformed EXAFS spectra and corresponding model fitting curves of NiO$_T$Pd15-T and NiO$_T$Pd30-T at Pd and Ni K-edges.

Table S2. The qualitative characteristics of the XANES spectra for the reference sample (Pd-CNT), control samples (NiO_TPd15 and NiO_TPd30) and experimental samples (NiO_TPd15-T and NiO_TPd30-T) at Pd K-edge.

Absorption edge	Sample	NiO_T	NiO_T-T	Pd-CNT	NiO_TPd15	NiO_TPd15-T	NiOTPd30	NiO_TPd30-T
Pd K-edge	X (eV)			24350	24349.5	24353.5	24349.5	24353.5
	ΔHMVN			0	0.053	0.036	0.045	0.041
	ΔHVN			0.119	0.109	0.051	0.096	0.063
	WMN			22.7	21.5	20	21.2	20.5
	ΔHX			0	0	0.01	0	0.006
Ni K-edge	X (eV)	8332.2	8332.2		8332.8	8332.8	8332.8	8332.8
	Y (eV)	8346	8346.3		8345.7	8346.5	8346.3	8346.5
	HC	1.61	1.611		1.305	1.658	1.525	1.731
	HX/WX	0.06	0.07		0.11	0.06	0.08	0.04

Table S3. EXAFS determined structural parameters of momometallic reference samples (Pd powder, Pd-CNT, Pd-T, Ni foil, NiO_T and NiO_T-T), control samples (NiO_TPd15 and NiO_TPd30) and experimental samples (NiO_TPd15-T and NiO_TPd30-T) at from model analysis on the corresponding EXAFS spectra Pd K-edge and Ni K-edges.

Absorption Edge	Sample		CN				χ (%)		R (Å)			
			Pd-O	Pd-Si	Pd-Pd	Pd-Ni	Si	Ni	Pd-O	Pd-Si	Pd-Pd	Pd-Ni
Pd K-edge	Reference	Pd powder	0		11.9						2.742	
		Pd-CNT	0.55		7.45				2.057		2.741	
		Pd-T	0.77		5.92				1.995		2.744	
	Control	NiO_TPd15	0.77		5.34	0.37	0	5.6	2.042		2.749	2.802
		NiO_TPd30	0.94		5.91	0.35	0	6.5	2.051		2.749	2.804
	Experimental	NiO_TPd15-T	0	2.89	2.47	0.95	45.8	15.1	2.141	2.368	2.788	2.864
		NiO_TPd30-T	0	2.14	2.98	0.81	36.1	13.7		2.365	2.766	2.842

Absorption Edge	Sample		CN						R (Å)				
			Ni-O1	Ni-O*	Ni-Ni^0	Ni-Si	Ni-O2	Ni-Ni2	Ni-O1	Ni-O*	Ni-Ni^0	Ni-Si	Ni-O2
Ni K-edge	Reference	Ni foil						11.9					
		NiOT	5.12				2.63	2.42	2.046				2.959
		NiO_T-T	5.64				1.57	2.56	2.045				2.902
	Control	NiO_TPd15	3.44	1.4	0.78		0	0.84	2.136	2.435	2.522		0
		NiO_TPd30	4.78				2.08	1.61	2.042				2.956
	Experimental	NiO_TPd15-T	5.52			0.69	2.14	2.97	2.037			2.465	2.899
		NiO_TPd30-T	5.98			0.44	1.67	2.51	2.042			2.449	2.898

Table S4. Calibrated product concentration of CO and CH_4 under 0.11 mbar CO_2 and mixing (CO_2+H_2) atmospheres from 323 K to 573 K for 12 mg of experimental samples (NiO_TPd15-T and NiO_TPd30-T) and reference samples (NiO_T-T and Pd-T). The unit of concentration is μmol/$g_{catalyst}$.

Feeding gas		CO_2							
Sample		NiO_T-T		Pd-T		NiO_TPd15-T		NiO_TPd30-T	
Products		CO	CH_4	CO	CH_4	CO	CH_4	CO	CH_4
Temp.	323	N/A	N/A	N/A	N/A	N/A	0.2	N/A	N/A
	373						0.9		
	423				0.4		1.5		2.0
	473			33.7	0.6	73.2	1.9	20.2	2.4
	523			54.8	0.8	334	3.3	356	3.9
	573	11.8		87.5	1.5	853	2.7	860	2.7

Feeding gas		CO_2 + $3H_2$							
Sample		NiO_T-T		Pd-T		NiO_TPd15-T		NiO_TPd30-T	
Products		CO	CH_4	CO	CH_4	CO	CH_4	CO	CH_4
Temp.	323	N/A	N/A	N/A	N/A	N/A	0.5	N/A	0.6
	373				8.2		4.1		4.7
	423		0.5		25.2	2.8	18.3		23.3
	473	7.1	12.3		86.5	241.5	110.3	287.3	100.3
	523	245.3	187.7	147.3	27.2	1208.2	530.6	1189.8	537.5
	573	2272.3	1083.2	636.8	92.2	3629.5	1905.1	2993.6	1727.9

4. Ambient Pressure X-ray Photoemission Spectroscopy (APXPS) results for the experimental

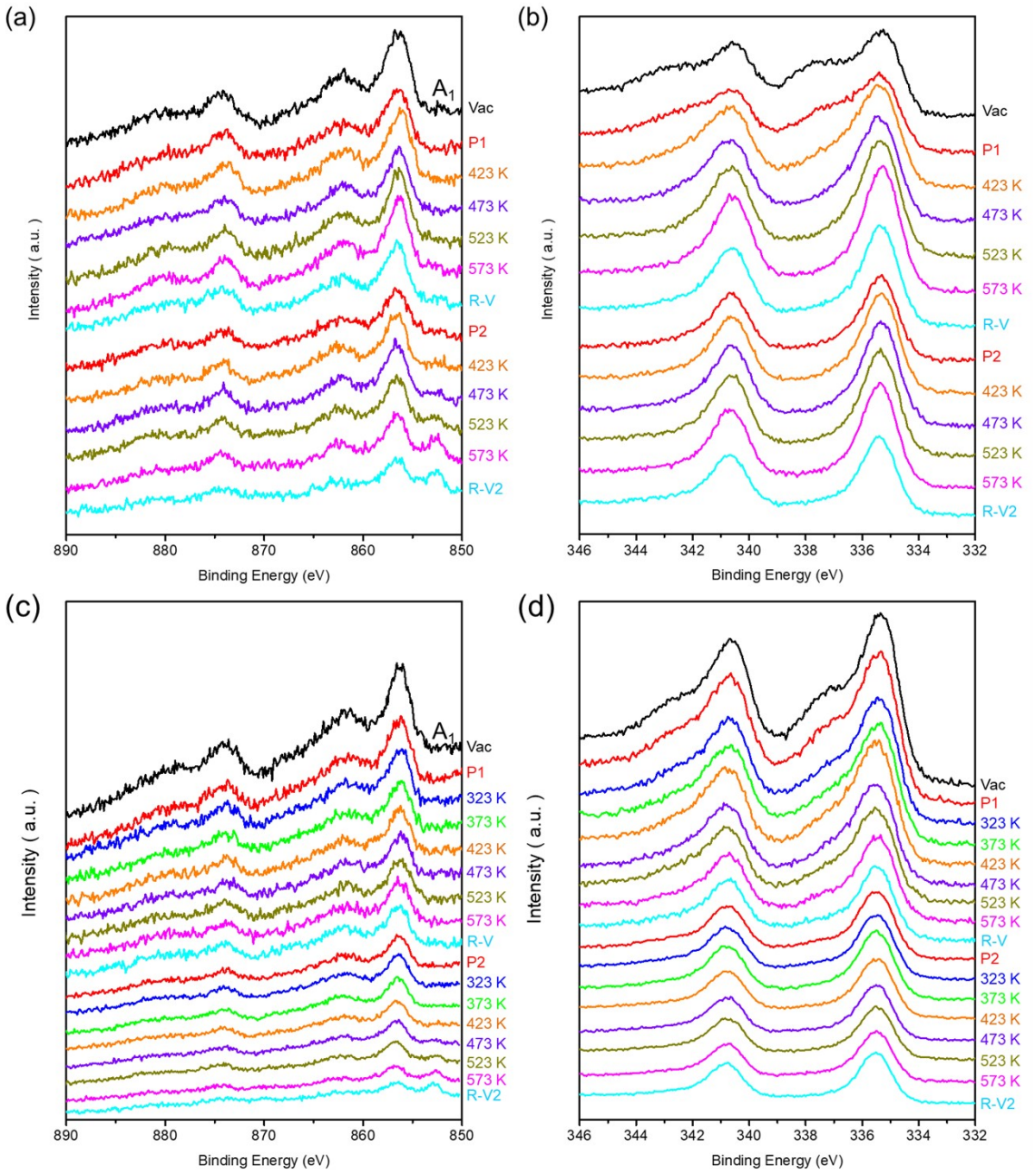

Figure S9. In-situ APXPS for NiO_TPd15-T NC at (a) Ni-2p and (b) Pd-3d orbitals and for NiO_TPd30-T NC at (c) Ni-2p and (d) Pd-3d orbitals. It operated at the initial state (**Vac**), under 0.11 mbar CO_2 (**P1**) and mixing gas (CO_2 and H_2, **P2**) from 323 to 573 K. **R-V** denotes back to room temperature (RT) and vacuum. (e) Corresponding Ni relative surface concentrations in the progress of CO_2RR with experimental samples (NiO_TPd15-T and NiO_TPd30-T).

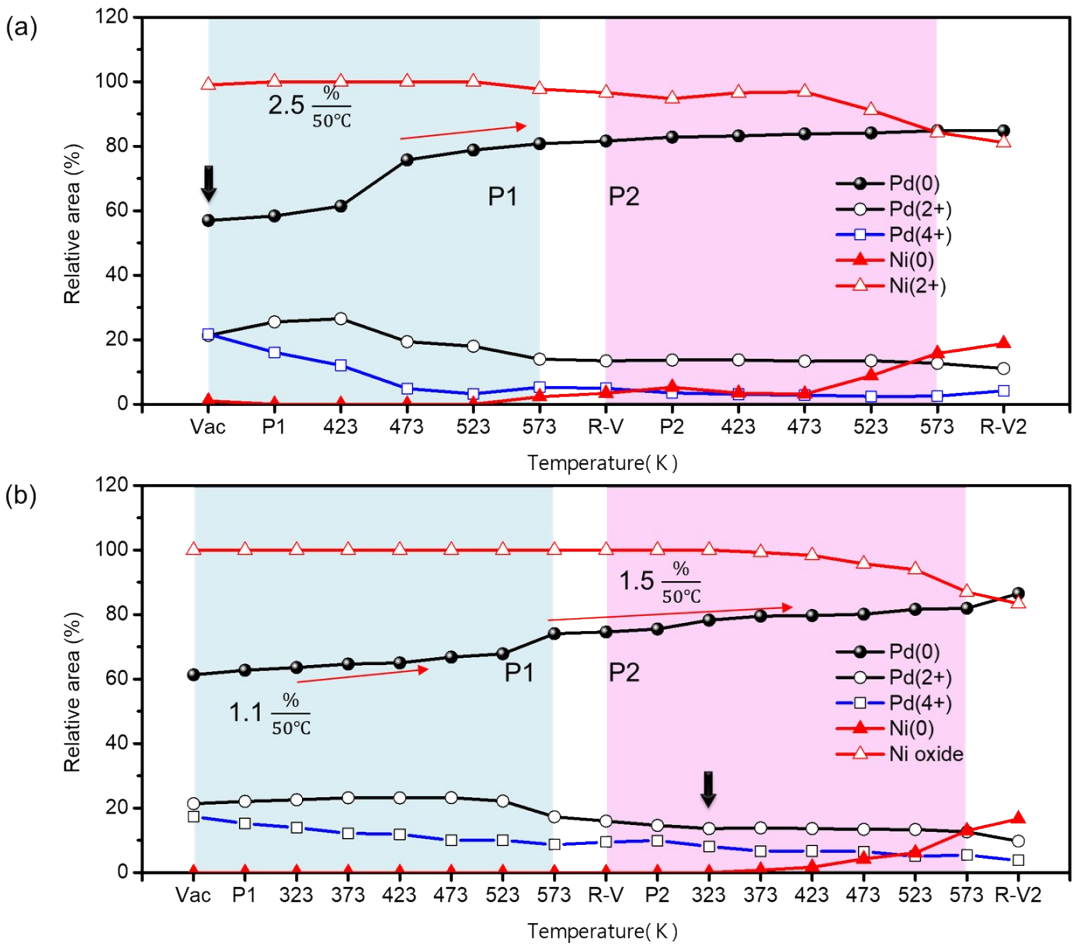

Figure S10. The variation of relative peak area between metallic Pd/Ni (solid) and metal oxide (hollow) in APXPS spectra and the corresponding schematic representation of reaction pathways for **(a)** NiO_TPd15-T and **(b)** NiO_TPd30-T NC. In-situ APXPS operated at 0.11 mbar ambient CO_2 (P1) and mixing gas (CO_2 and H_2, P2) from RT to 573 K.

Table S5. The changes of CO and CH_4 production yields with the ambient conditions are compared with that of the Ni and Pd chemical states in NiO_TPd15-T.

State	Ni metal (%)	Ni oxide (%)	Pd metal (%)	Pd2+ (%)	Pd4+ (%)	CO	CH_4
Vac	1.01	98.99	56.96	21.30	21.74		0.2
P1	0	100	58.36	25.54	16.1	N/A	0.9
423	0	100	61.42	26.52	12.06		1.5
473	0	100	75.75	19.4	4.85	73.2	1.9
523	0	100	78.8	17.98	3.22	334.4	3.3
573	2.31	97.69	80.79	13.96	5.26	852.6	2.7
R-V	3.39	96.61	81.62	13.46	4.92		
P2	5.27	94.73	82.8	13.68	3.52		
323						N/A	0.5
373							4.1
423	3.45	96.55	83.19	13.72	3.09	2.8	18.3
473	3.13	96.87	83.84	13.36	2.8	241.5	110.3
523	8.84	91.16	84.1	13.5	2.41	1208.2	530.6
573	15.78	84.22	84.82	12.69	2.49	3629.5	1905.1
R-V2	18.82	81.18	84.76	11.05	4.19		

Table S6. The changes of CO and CH_4 production yields with the ambient conditions are compared with that of the Ni and Pd chemical states in NiO_TPd30-T.

State	Ni metal (%)	Ni oxide (%)	Pd metal (%)	Pd2+ (%)	Pd4+ (%)	CO	CH4
Vac	0	100	61.31	21.35	17.35		
P1	0	100	62.73	22.06	15.2		N/A
323	0	100	63.58	22.53	13.89	N/A	
373	0	100	64.66	23.19	12.14		
423	0	100	65.01	23.13	11.87		2.0
473	0	100	66.78	23.23	9.99	20.2	2.4
523	0	100	67.83	22.16	10.01	356.0	3.9
573	0	100	74.07	17.28	8.65	860.0	2.7
R-V	0	100	74.59	15.96	9.45		
P2	0	100	75.49	14.6	9.91		
323	0	100	78.24	13.64	8.12		0.6
373	0.75	99.25	79.52	13.84	6.65		4.7
423	1.66	98.34	79.68	13.64	6.68		23.3
473	4.26	95.74	80.11	13.39	6.5	287.3	100.3
523	6.11	93.89	81.6	13.34	5.05	1189.8	537.5
573	12.99	87.01	81.94	12.61	5.42	2993.6	1727.9
R-V2	16.63	83.37	86.5	9.74	3.76		